

# The Synergy of CFD and Experiments in Aerodynamics Research at Cranfield University, Shrivenham

A. J. Saddington, K. Knowles and N. J. Lawson

Aeromechanical Systems Group,  
Department of Aerospace, Power and Sensors,  
Cranfield University, RMCS, Shrivenham,  
Swindon, Wiltshire, SN6 8LA, UK  
k.knowles@rmcs.cranfield.ac.uk

**Keywords:** LDV, PIV, CFD, supersonic, jet, transonic, cavity, racecar

## Abstract

This paper discusses how the combined use of computational fluid dynamics and experimentation has been applied to three particular fluid dynamics problems: high-speed turbulent jet flow, transonic cavity flows and open-wheeled race car aerodynamics. In each case knowledge gathered from one analysis technique has been used to assist in the application of the second technique thereby enabling greater understanding of the flow physics being studied than would have been possible through the isolated use of one or other methodology.

## 1 Introduction

For some time now, aerodynamics research carried out at Cranfield University's Shrivenham Campus has made use of both experimental and numerical methods. The combination of these two disciplines has enabled greater understanding of the flow physics being studied than would have been possible through either a purely experimental or purely numerical approach. Using examples of recent research projects, this paper will discuss the synergistic role that CFD and experiments have had in our aerodynamics research programme.

Early combined CFD and experimental research was primarily driven by the need for CFD validation e.g. [1]. With computational resources limited, the experimental results were primarily used to validate the CFD models. The main objective was to give globally similar results to those measured in the experiments. The CFD was then used to reveal limited extra information on the flowfield.

More recently, improved computational resources have enabled refinements to the CFD models. Whilst CFD validation is still important, these models have provided additional insight into the physical processes involved, which were not discernable from the experimental measurements.

## 2 High-speed jet research

The rate at which a supersonic jet mixes with the surrounding ambient fluid is important for many aerospace applications, notably in jet aircraft and rocket propulsion. For supersonic jets the generation of streamwise vortices appears to be beneficial in improving mixing [2] and schemes have been investigated using vortex generators, tabs [3] and other intrusive devices. This work [4,5] presents a numerical and experimental study of mixing in underexpanded, supersonic turbulent jets issuing from axisymmetric and castellated nozzles into quiescent conditions.

Experimental measurements using laser doppler velocimetry (LDV) and pitot probe measurements [6] along the jet centreline at a nozzle pressure ratio (NPR = nozzle total to ambient static pressure ratio) of 4 indicated that the

castellated nozzles entrained more mass flow into the jet than a simple convergent nozzle. The CFD models verified that this was the case but crucially also provided a physical explanation of the entrainment mechanism that would have been very difficult to deduce from the available experimental data.

## 2.1 Nozzle design

Three castellated nozzles with convergent profiles and an exit diameter,  $D$  of 29.4 mm were investigated (Fig. 1). Each nozzle had four regularly spaced castellations. The difference between the three nozzles was confined to the geometry of the gap between each castellation. The first nozzle (regular) had castellations cut by a radial line from the centre of the nozzle, as shown by the inner region of Fig. 2. The 'outer region' of Fig. 2 indicates alternative tooth designs (for all four teeth); radial position is as the 'inner region'. The second nozzle (divergent chamfered) had castellations cut such that the gap between each nozzle was divergent in profile, as indicated by the '\*' on the outer region of Fig. 2. The third nozzle (convergent chamfered) had castellations cut such that the gap between each profile was convergent in profile, as indicated by the '\*\*' on the outer region of Fig. 2. The plain axisymmetric nozzle was of the same overall geometry as the castellated ones but with the gaps between the teeth 'filled in' [7]. The mixing enhancement obtained from the three castellated nozzle geometries was to be compared with the axisymmetric convergent nozzle [7].

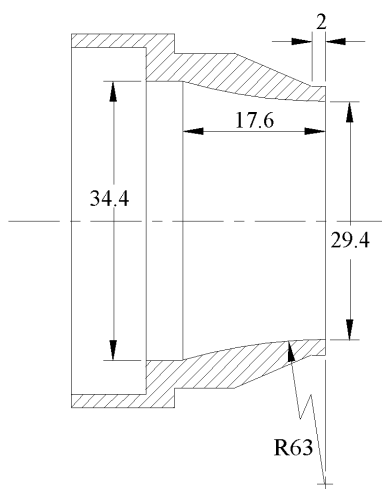


**Figure 1:** Nozzle geometry showing the internal profile.

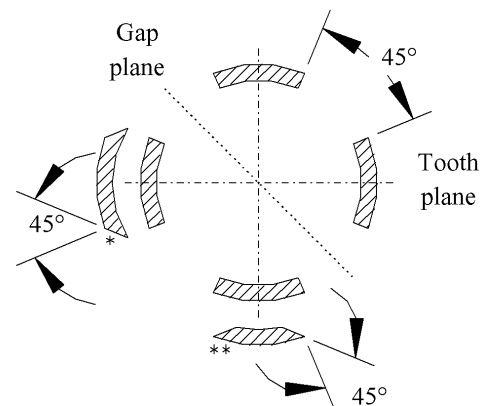


**Figure 2:** Nozzle castellation configurations. Hatched boxes indicate locations of teeth in nozzle lip: (\*) alternative profile for divergent chamfered castellations; (\*\*) alternative profile for convergent chamfered castellations.

## 2.2 Experiments

Experiments were conducted in a nozzle test cell at Shrivenham (Fig. 3). Data were collected for a NPR of 4. Three-dimensional LDV measurements were taken of the flow from the castellated nozzles. Seeding of the jet was by direct injection from a TSI six-jet seeder into the nozzle plenum chamber using JEM Hydrosonic seeding fluid.

Measurement traverses were made along the nozzle centreline,  $x$ . Probe access limited data collection to the first 10D from the nozzle exit plane. The LDV measurements were estimated to be accurate to  $\pm 1\%$  of velocity based on the sample time and frequency. Additional comparative data were taken from centreline LDV measurements of the plain axisymmetric nozzle [4] and pitot probe measurements of the convergent chamfered castellated nozzle [6, 8] made previously under the same test conditions.

## 2.3 Numerical Model

The CFD model was developed using the Fluent commercial code (Version 5.5). The computational domain consisted of a three dimensional hexahedral mesh with approximately 250,000 to 450,000 cells depending on the test conditions. Only one quarter of the geometry was modelled since each nozzle has two axes of symmetry. The inlet plane was approximately 1D upstream of the nozzle exit, the outlet plane was at about 50D downstream and the radial boundary diverged from 2D at the upstream end to more than 10D downstream.

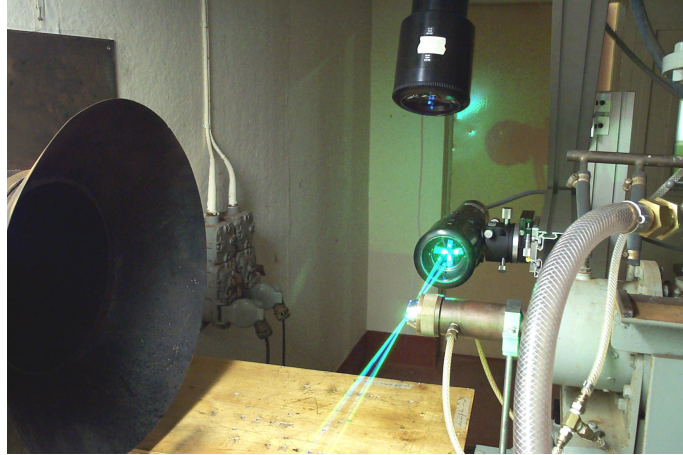


**Figure 3:** LDV measurements in the nozzle test cell.

The boundary condition for the nozzle inlet was set as a pressure inlet with a prescribed total pressure, static pressure, total temperature and turbulence intensity. The turbulence intensity,  $T_i$  at nozzle inlet in the CFD model was adjusted to give the same nozzle exit turbulence intensity as the experiments (approximately 4%). The experimental  $T_i$  was derived from the rms velocity data measured by the LDV technique. The turbulence length scale was set as 7.5% of nozzle radius [9]. The farfield boundary was set as a pressure outlet with a prescribed static pressure and static temperature.

Turbulent calculations were performed using the RNG  $k-\varepsilon$  turbulence model [10], which has been shown to be suitable for modelling under-expanded jets [11]. Initial axisymmetric calculations were conducted on a mesh of 14700 cells. Three stages of mesh adaption, based on density gradients greater than  $1 \times 10^{-5}$  (to capture the shear layer) and Mach numbers greater than 1.0 (to capture the shock core), were then performed. This reduced the grid spacing in the shock cell regions from 2 mm to 0.25 mm. Three stages of mesh adaption were sufficient to ensure a grid-independent solution [7].

## 2.4 Mixing Enhancement

Both the experimental measurements and the CFD model indicated that the castellated nozzles produce jets with shorter shock cells than the axisymmetric jet (Table 1), however, it was still to be determined if this translated into enhanced jet mixing. For the purposes of the study, jet mixing was determined by a numerical integration of the mass flow rate passing through planes normal to the jet axis at various streamwise positions ( $x/D = 2.5, 5, 7.5, 10, 15, 20$ ). The edge of the integration plane was chosen to be where  $M = 0.06$ .

At  $x/D = 2.5$  all three castellated nozzles showed an increased mass flow rate in the jet of between 6% and 9% when compared with the axisymmetric jet. At  $x/D = 5$  this has increased to approximately 13% for the regular and divergent chamfered castellated nozzles. The convergent chamfered castellated nozzle showed a reduced mixing enhancement of only 2%. At  $x/D = 7.5$  the level of mixing enhancement started to deteriorate in the other nozzles as well, the divergent chamfered castellated nozzle offering the best enhancement with a 10% increase in mass flow rate. The mixing enhancement continued to reduce as downstream distance was increased until, beyond  $x/D = 15$ , the mass flow rate in the axisymmetric jet exceeds that in the jets from the castellated nozzles.

In order to gain some insight into the mechanism responsible for the mixing enhancement, contour plots of the Mach

$x/D$	Axisymmetric		Regular		Convergent		Divergent	
	$\dot{m}$ ( $\text{kg s}^{-1}$ )	$\dot{m}$ ( $\text{kg s}^{-1}$ )	$\dot{m}$ ( $\text{kg s}^{-1}$ )	% change	$\dot{m}$ ( $\text{kg s}^{-1}$ )	% change	$\dot{m}$ ( $\text{kg s}^{-1}$ )	% change
0.0	0.638	0.642	0.6	0.6	0.643	0.8	0.640	0.3
2.5	0.745	0.811	8.9	8.9	0.796	6.8	0.790	6.0
5.0	0.867	0.975	12.5	12.5	0.884	2.0	0.982	13.3
7.5	1.012	1.080	6.7	6.7	1.011	-0.1	1.110	9.7
10.0	1.172	1.192	1.7	1.7	1.166	-0.5	1.220	4.1
12.5	1.377	1.361	-1.2	-1.2	1.325	-3.8	1.417	2.9
15.0	1.582	1.547	-2.2	-2.2	1.557	-1.6	1.541	-2.6
17.5	1.795	1.770	-1.4	-1.4	1.749	-2.6	1.794	-0.1
20.0	2.025	1.982	-2.1	-2.1	1.961	-3.2	2.016	-0.4
25.0	2.476	2.458	-0.7	-0.7	2.440	-1.5	2.483	0.3
30.0	2.953	2.916	-1.3	-1.3	2.897	-1.9	2.937	-0.5

**Table 1:** CFD prediction of the mass flow rate of the four nozzles at various streamwise planes.

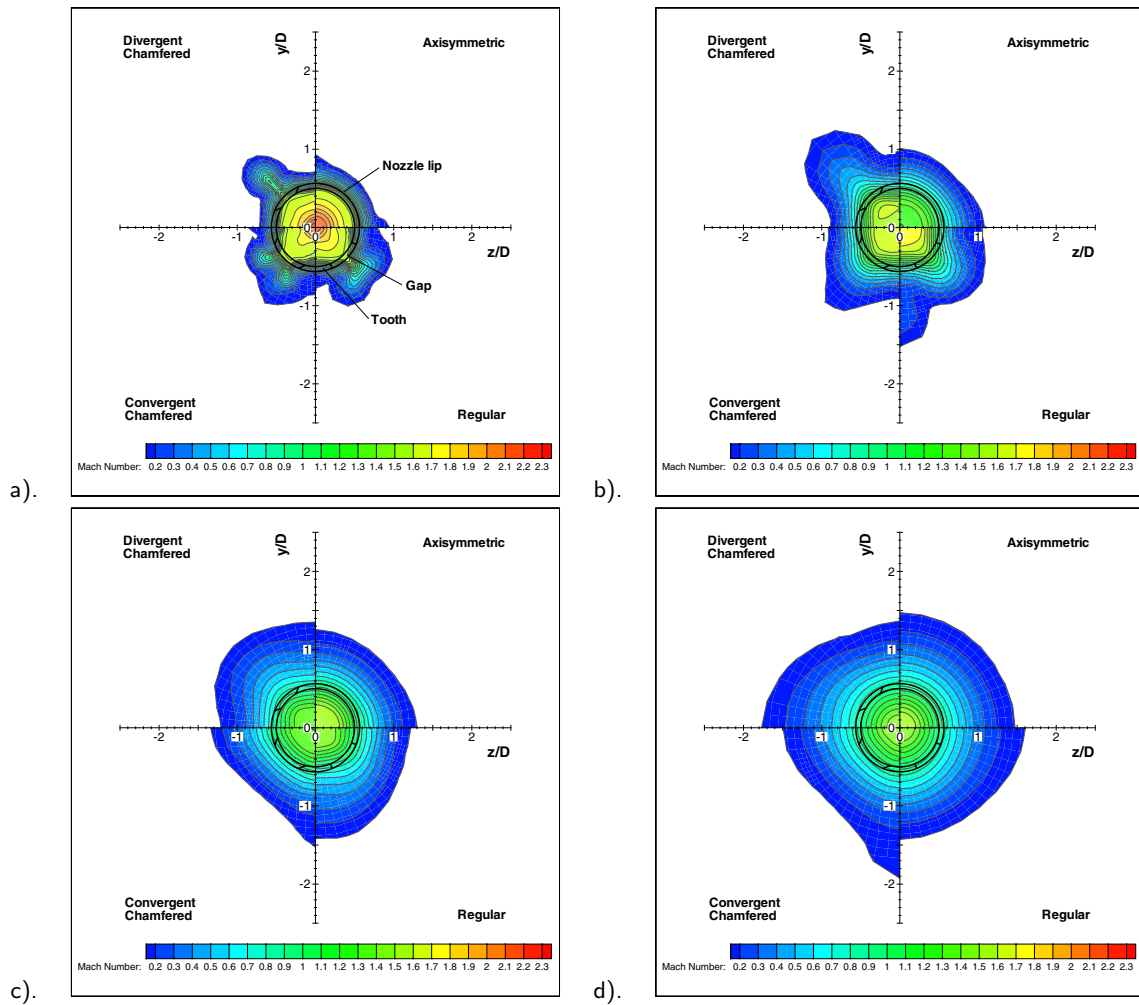


**Figure 4:** CFD-predicted Mach number contours at various distances downstream of the nozzle exit: a).  $x/D = 2.5$ ; b).  $x/D = 5$ ; c).  $x/D = 7.5$ ; d).  $x/D = 10$ .

number at each streamwise plane were examined for the CFD data (Fig. 4). At  $x/D = 2.5$ , the cross-sectional shapes of the jets are very different. The divergent chamfered nozzle produces a jet with a lobe of high velocity fluid, which has been ejected radially through the gap in the castellations. Similar fluid ejections, but of slightly different shapes were observed for the other two castellated nozzle designs.

The CFD model showed that the increased jet mixing produced by the castellated nozzles appeared to be due to differential expansion of the jet fluid in the gap and tooth regions as it leaves the nozzle exit. This differential expansion created a distorted jet cross section which presented a larger surface area to the ambient air, thus enabling more rapid entrainment. The mixing enhancement was, however, confined to the nearfield flow ( $x/D < 10$ ). At greater streamwise distances viscous dissipation appeared to cause the entrainment mechanism to decay resulting in mixing rates lower than an axisymmetric jet with final mass flow rates similar in each case. Although the mixing enhancement could be determined experimentally, the entrainment mechanism responsible could only be determined from the CFD.

### 3 Transonic cavity flow

Transonic cavity flows over rectangular cavities are of particular relevance to aircraft weapons bays. For cavity length to depth ratios less than about 10 the flow is characterised by intense acoustic tones and flow unsteadiness. We present here numerical modelling and particle image velocimetry (PIV) measurements of a transonic cavity ( $M_\infty = 0.85$ ) with a length to depth ratio,  $L/D$  of 5 [12]. Here the numerical model is used to aid optimisation of the PIV set-up.

#### 3.1 Numerical model

The CFD model was completed using commercial software GAMBIT + Fluent 6. The computational grid was created from 86000 uniform quadrilateral cells with a distribution of  $320 \times 65$  cells within the cavity. The domain was designed to be geometrically similar to the wind tunnel test section. Thus, the upper and lower surface of the tunnel were modelled with wall boundary conditions whilst the inlet and outlet conditions were modelled as the pressure far-field or free air condition. The flow problem was solved using the unsteady coupled solver and realisable  $k-\epsilon$  turbulence model. The  $k-\epsilon$  family of turbulence models was selected as a number of previous studies have shown it to perform well for flows with high shear and regions of recirculation.

#### 3.2 Experimental Model

PIV data were taken from inside an all glass cavity of 160 mm length, 80 mm width and 32 mm depth. The cavity is made from 5 mm thick glass and is mounted in a modified tunnel wall. Due to the design of the transonic wind tunnel test section it was not possible to image the entire cavity and into the freestream and the top 3 mm inside the cavity could not be mapped due to the presence of a metal flat plate. Details of the experimental set up are given in Ritchie [12].

An in-house designed seeder injected a 5% glycerol and water solution into the contraction section of the wind tunnel for the PIV measurements. The seeder consisted of an atomiser with 25 selectable jets and was supplied from the main tunnel air supply.

PIV images were recorded using a Kodak ES1.0 CCD with a 105 mm Micro-Nikor lens and a New Wave Gemini double pulsed Nd:YAG laser. Sets of 70 images were taken for each run. Figure 5 shows a typical PIV image. Data processing of the sets of 70 images was carried out using the TSI software UltraPIV with the Hart algorithm [13]. The performance of the UltraPIV algorithm, however, was found to be poor in regions of low seeding density. Therefore an in-house algorithm was also developed based on correlation averaging as proposed by Meinhart [14]. This was used to process the same 70 image set.

#### 3.3 Experimental Optimisation

Lawson *et. al.* [15] have described an optimisation method for a double pulsed PIV experiment which can be applied to autocorrelation or cross correlation analysis. They have shown that in order to retrieve a valid velocity vector from an interrogation region there exists a strong interdependence between the dynamic range,  $D_r$ , of the flow defined by:

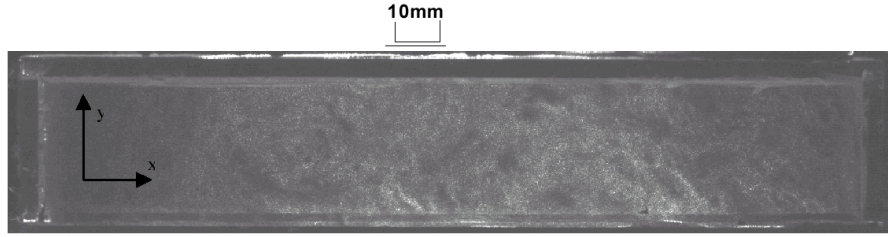


Figure 5: Typical instantaneous PIV particle image.

$$D_r = \left| \frac{V_{\max}}{V_{\min}} \right| \quad (1)$$

where  $V_{\max}$  and  $V_{\min}$  are the maximum and minimum velocities measured in the flow plane and the velocity gradient strength,  $\varphi$  defined by:

$$\varphi = \frac{V_2 - V_1}{V_{\max}} \quad (2)$$

Here,  $V_2 - V_1$  is the velocity change across the interrogation region. A high dynamic range requirement necessarily restricts the strength of the velocity gradient in a chosen region and vice versa. The latter condition is crucial to the design of a PIV experiment for use in transonic and supersonic flows. In any given experiment, other parameters critical to the PIV system's performance include the seeding density and corresponding particle image density,  $N_i$  and the interrogation region size relative to particle image size,  $D/d$ . All these parameters must be considered when optimising the correlation performance whether using conventional correlation or the Hart correlation. In the latter case, an equivalent number of particle images must be used by considering the surrounding interrogation regions.

With *a-priori* knowledge of  $D_r$ ,  $\varphi$  and  $V_{\max}$ ,  $D/d$  and  $N_i$ , it is possible to use the method to determine a laser pulse separation,  $\Delta t$  for a PIV experiment which will ensure that, on average, from a series of experiments at least 50% of valid vectors will be obtained from a 'worst case' interrogation region in the flow. The experiments are then defined as being optimised.

The CFD predictions provide the *a-priori* knowledge of  $D_r$ ,  $\varphi$ ,  $V_{\max}$  and  $V_{\min}$ , where the spatial resolution requirement will determine the parameters  $D/d$  and  $N_i$  from the PIV experiment. The optimisation method will then yield a recommended magnification,  $M$  and pulse separation,  $\Delta t$ .

The system magnification is defined in terms of the ratio of object and image distances and is that which is required to capture the flow area. The spatial resolution,  $L$  of the system is defined by:

$$L = D/M \quad (3)$$

where  $D$  is the interrogation region length and the particle image size,  $d$  is dependent on the depth of field and laser power of the system.

The CFD provided the *a-priori* information from inside the cavity listed in Table 2. The PIV requires a spacial resolution of 1.5 mm. This leads to the experimental PIV values listed in Table 3.

Therefore if the particle image displacement is restricted to 20% of  $D$  and applying the optimisation method [15], yields a maximum allowable value of  $\varphi D_r = 1.5$ , which corresponds to  $\varphi = 21\%$  given  $D_r = 7$ . Also, a magnification of  $M = 1/16$  must be used and a pulse separation  $\Delta t = 30$  ms. Since the maximum allowable value of  $\varphi = 21\%$  is greater than the CFD predicted value of  $\varphi = 15\%$ , this means the PIV experiment will have sufficient performance to ensure a minimum of 50% of valid vectors, on average, inside this region where the velocity gradients and dynamic range are highest.

Parameter	Value
$V_{\min}$ ( $\text{ms}^{-1}$ )	-5
$V_{\max}$ ( $\text{ms}^{-1}$ )	35
$\underline{V}_2 - \underline{V}_1$ ( $\text{ms}^{-1}$ )	5
$D_r$	7
$\varphi$ (%)	15

**Table 2:** CFD *a-priori* values.

Parameter	Value
L (mm)	1.5
CCD size (pixels)	1000 <sup>2</sup>
Particle image size (pixels)	3
D/d	10
$N_i$	5

**Table 3:** Experimental parameter values.

### 3.4 Results

Figures 6 and 7 show time-averaged vector maps output from the PIV data processing from the Hart and the correlation averaging algorithms. The results from the Hart algorithm do not show any substantial recirculation regions contrary to predictions by the CFD model. In contrast the results from the in-house correlation averaging algorithm show a distinct large scale recirculation inside the cavity as can be seen in the PIV image of Figure 5. Lower than expected seeding levels would not provide the performance predicted by the optimisation method which assumed a minimum of 5 particle images per interrogation region. The correlation averaging algorithm, however, ensures greater than 5 particles images per interrogation region as the 70 images set on average accumulates more than 5 particle images in each interrogation region.

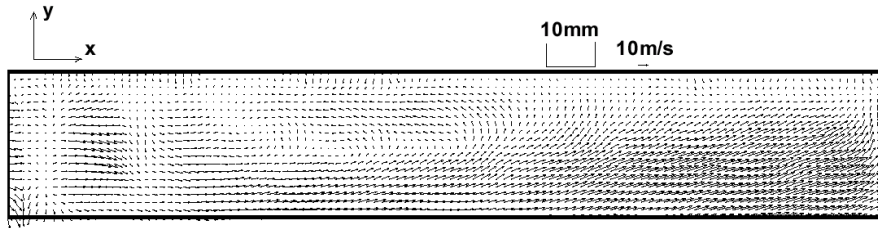


**Figure 6:** TSI code processed time averaged PIV vector map (70 Image average).

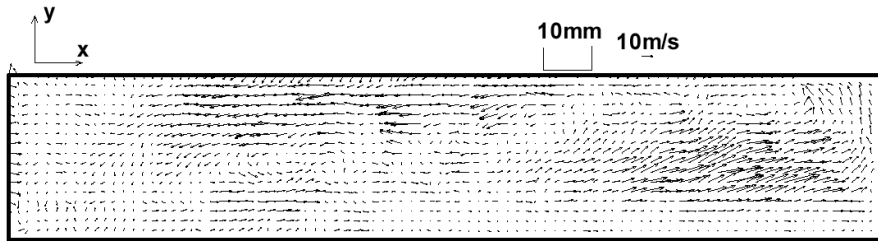


**Figure 7:** In House code processed time averaged PIV vector map (70 Image average).

The improved performance of the correlation averaging method is further illustrated in a U component centreline plot of velocity shown in Figure 8. In this case the TSI data has a greater deviation than the correlation averaged results when compared to the CFD prediction. Therefore optimisation of a given PIV system requires not just *a-priori* knowledge of the flow to specify variables such as M and  $\Delta t$ , but also careful control of variables such as seeding and judicious choice of the data processing algorithms for a given flow.

## 4 Open-wheeled racecars

Ground simulation and wheel rotation are known to be essential for accurate automotive testing [16], particularly for open-wheeled racecars. With this type of vehicle, ground effects and large unfaired wheels dominate their aerodynamic characteristics. Every care must be taken to ensure that the wheels are modelled correctly both in experimental testing

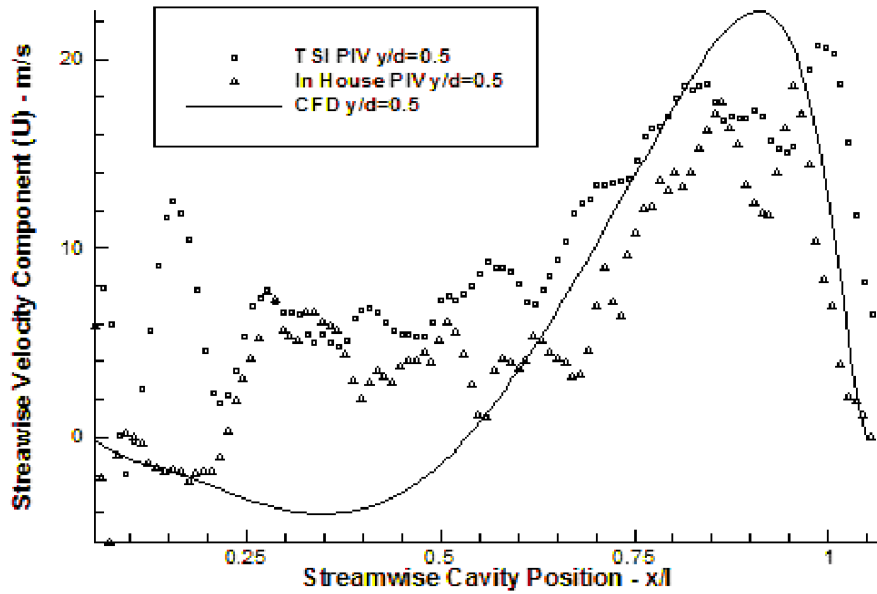


Figure 8: Streamwise Velocity Profile -  $y/d=0.5$ .

and computational simulation. Previous evaluations of the capability of CFD to model wheel flows [17–19] used the surface pressure and force data published by Fackrell [20,21] as their main validation criteria.

CFD models enable researchers to investigate physical processes that may be impossible to reproduce experimentally. In our work the investigation concentrated on the effect of using external wheel support struts during racecar wind tunnel testing [22]. The struts are used to mechanically decouple the car body from the ground whilst still allowing the wheels to rotate. Ideally the support struts should be aerodynamically neutral, however, this is not always the case.

An experimentally validated CFD model of an isolated racecar wheel and strut was used to quantify the aerodynamic interference effects between the two. The virtual environment of the CFD model enabled the support strut to be easily removed, something that could not have been carried out experimentally.

#### 4.1 Experiments

A 40% scale (263 mm diameter), non-deformable Champ Car front wheel assembly was chosen along with its associated support sting. The experimentally tested sting was of aluminium beam section with a symmetrical aerofoil profile. It supported a 50 N load cell, oriented to measure drag force, to which the wheel was attached. The aerofoil profile was extended to the wheel by shrouding the load cell with carbon fibre. The instrumentation cabling was shielded from the freestream air by routing it inside the sting. No vertical force, other than that due to the weight of the components, was applied during testing and no problems were encountered with wheel lift. The experimental set-up is shown in Figure 9.

The LDV measurements were made using a two-component and a single-component, 1m focal length, Dantec FibreFlow probes mounted to a three-component traverse. Data acquisition was carried out by three BSA enhanced signal processors, with all equipment centrally controlled by Dantec Burstware software.

The experimental set-up was tested at  $20 \text{ ms}^{-1}$ , corresponding to a Reynolds number (based on wheel diameter) of  $3.69 \times 10^5$ . LDV measurements were made in four vertical planes oriented perpendicular to the freestream flow. Traverse access confined each plane to being a 250 mm square, centred about the longitudinal centreline of the wheel. The planes were located at 10, 25, 50 and 100 mm downstream of the rearmost part of the wheel and contained identical grids of 441 equally-spaced data points. All three velocity components were simultaneously sampled over a 15 second period yielding 2500 samples for each component at each point. When processed, these data subsequently provided time-averaged three-dimensional velocity results.

## 4.2 Numerical model

The wheel and sting assembly was placed in a rectangular domain with the inlet 5 wheel diameters upstream, outlet 16 wheel diameters downstream, a width of 10 and a height of 5 wheel diameters. The interior of the sting was also meshed to allow it to be removed from the solution domain by allowing fluid to flow through it, thus eliminating the need to generate an entirely new mesh for that section of the study.

The only significant deviation from the experimental geometry was made at the tyre contact patch. Difficulty was encountered in maintaining high cell quality when modelling the near line-contact between the rolling road and non-deformable tyre. Therefore, the wheel was slightly truncated by raising the ground plane by 0.8mm. This increased the size of the contact patch and greatly improved the cell skewness in this area. The final mesh was of the order of 0.93 million cells. Figure 10 shows the surface mesh on the wheel and sting assembly.



Figure 9: Experimental Set-up

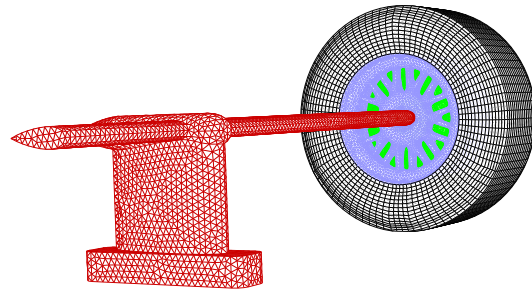


Figure 10: CFD Surface Mesh of Wheel Assembly and Support Sting

The boundary conditions of the CFD simulation were chosen to be representative of those of the experiment. A uniform flow with a velocity of  $20 \text{ ms}^{-1}$  was specified at the inlet and standard atmospheric pressure specified at the outlet. The rolling road and wheel components were modelled as translating and rotating walls respectively, all with a linear velocity of  $20 \text{ ms}^{-1}$ . When simulating the wheel and sting, the sting surface was specified as a wall with the no-slip condition applied. When testing the wheel without the sting, the latter's surface was represented by an interior condition, which did not impede flow. The mesh inside the sting was solved as a fluid, effectively removing the sting from the domain. Symmetry planes represented the remaining domain boundaries. Simulations were run with the  $k-\omega$  turbulence model.

## 4.3 Validation

The mean drag force calculated from the experimental data was non-dimensionalised by the frontal area of the wheel. The drag coefficient,  $C_D$  predicted by the CFD simulation was 0.638, which was 6.2% lower than the measured value of 0.680.

Care should be exercised when using force data as the sole accuracy measure [23] but the good experimental velocity correlation supported the validity of this prediction. This was further reinforced by inspection of the circumferential static pressure coefficient,  $C_p$  on the centreline of the tyre surface, Figure 11. Although surface  $C_p$  was not measured experimentally, comparison can be made with the work of Hinson [24]. This presented the pressure coefficients on the surface of a Formula One wheel, measured using transducers mounted within. Comparison was made with results taken from tests at the same Reynolds number as, and using a geometrically similar wheel to, this investigation. The results show good correlation and illustrate several important features. CFD predicted the separation  $22^\circ$  late at  $244^\circ$  as opposed to  $266^\circ$  measured by Hinson. Also, the base pressure was under-predicted just downstream of separation. Both factors would lead to an under-prediction of drag coefficient and are believed to be responsible, along with experimental errors, for the discrepancy seen in this study.

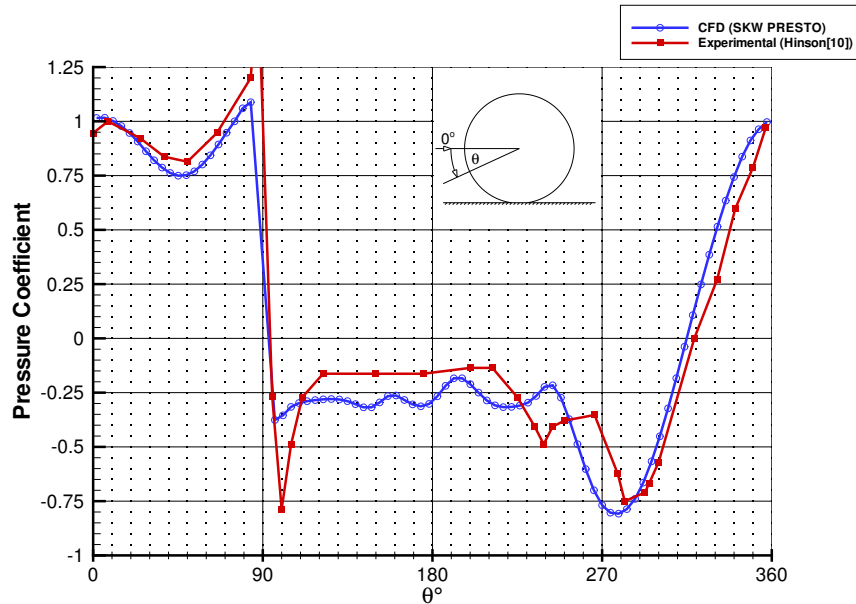


Figure 11: Circumferential Pressure Distribution on the Tyre Centreline

#### 4.4 Support Sting Effects

Once the CFD model had been validated, it could be used to determine the effect of the support sting on the flow in proximity to the wheel. Figure 12 shows velocity vector plots from the CFD investigations with and without the support sting. The model used throughout the study enabled the sting to be removed without modification to the mesh. The solver settings could, therefore, remain constant, thus improving comparison.

The main difference (seen in the 10 mm and 25 mm planes) is the presence of a contra-rotating upper vortex pair in the no-sting results, as opposed to the single structure with the sting present. This would suggest that the presence of the sting suppresses the formation of the upper left vortex. The upper structures appear to breakdown quicker when the sting is not present and are absent in the 100 mm plane.

With regard to the two vortices close to the ground (known as 'jetting' vortices), the left structure is the larger of the two and is located higher and closer to the wheel centreline in the no-sting results. This is in contrast to the results noted in the presence of the sting.

Inspection of the remaining data showed that removal of the support sting resulted in:

- A wheel drag reduction of 2%;
- An increase in wheel lift of 16%;
- A reduction in mass flow-rate through the wheel of 83%;
- A delay of separation by  $4^\circ$ , on the wheel centreline.

The slight drag reduction appears to correlate with the later separation, whilst the additional upper vortex agrees with the increase in lift. Flow through the wheel is from right to left, therefore the results suggest that the sting forces more flow to pass through the wheel than would otherwise occur.

This study has shown how an experimentally validated CFD model of an isolated racecar wheel and strut can be used to quantify the aerodynamic interference effects between the two. The virtual environment of the CFD model enabled the support strut to be removed easily, something that could not have been carried out experimentally.

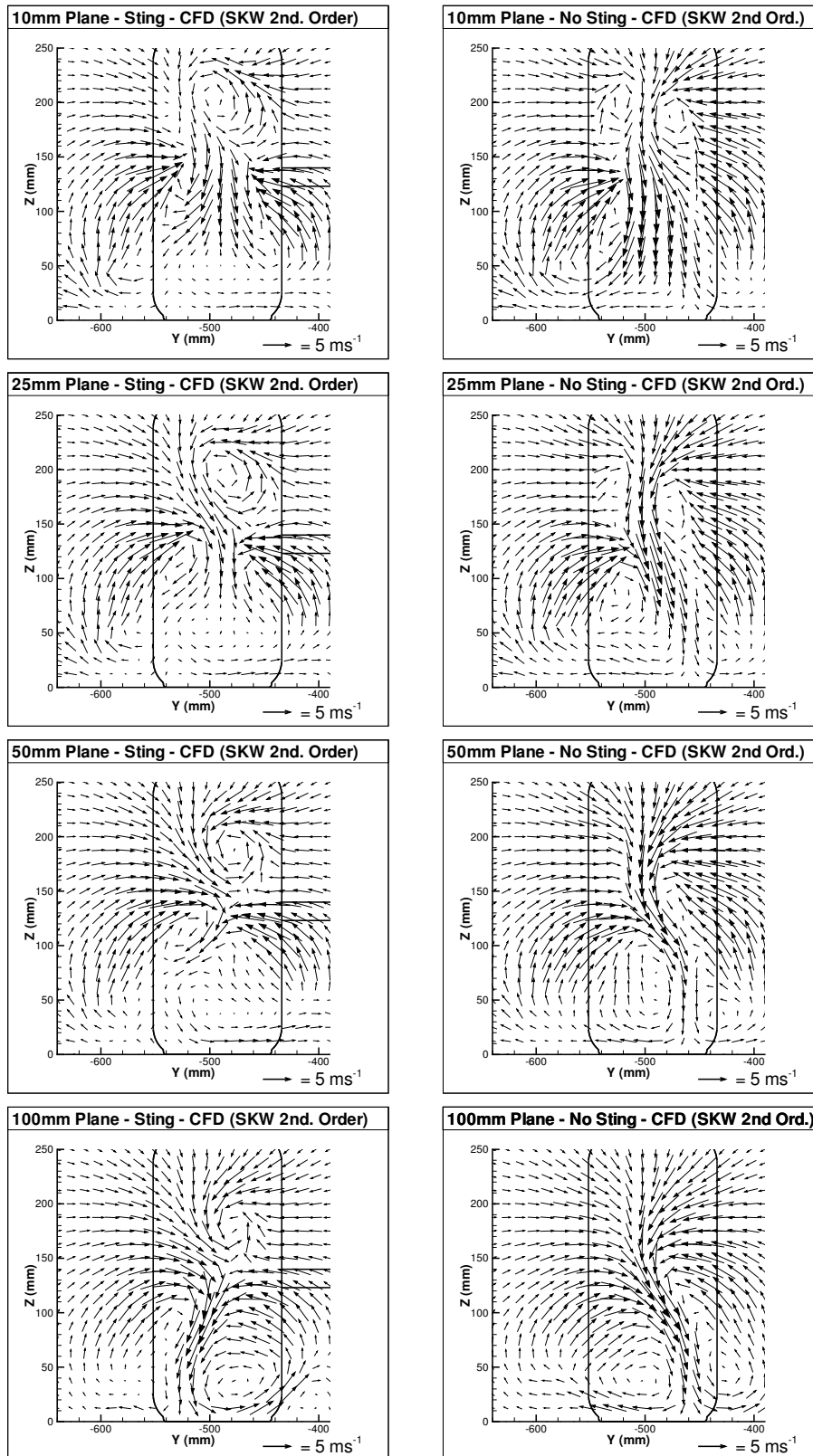


Figure 12: In-Plane Velocity Vectors (Sting - No Sting CFD Comparison)

## 5 Conclusions

In this paper we have illustrated how the combined use of computational fluid dynamics and experimentation has been applied to three particular fluid dynamics problems: high-speed turbulent jet flow, transonic cavity flows and open-wheeled race car aerodynamics. In each case knowledge gathered from one analysis technique has been used to assist in the application of the second technique thereby enabling greater understanding of the flow physics being studied than would have been possible through the isolated use of one or other methodology. The authors would like to acknowledge the work of Simon Ritchie and Robin Knowles in support of this paper.

## References

- [1] Knowles, K. and Bray, D., "Computation of Normal Impinging Jets in Cross-flow and Comparison with Experiment," *International Journal of Numerical Methods in Fluids*, Vol. 13, No. 10, December 1991, pp. 1225–1233.
- [2] Samimy, M., Reeder, M. F., and Zaman, K., "Supersonic Jet Mixing Enhancement by Vortex Generators," *AIAA/SAE/ASME/ASCE 27th Joint Propulsion Conference*, Sacramento, CA, USA, 24–26 June 1991, No. 91-2263.
- [3] Samimy, M., Zaman, K. B. M. Q., and Reeder, M. F., "Effect of Tabs on the Flow and Noise Field of an Axisymmetric Jet," *AIAA Journal*, Vol. 31, No. 4, April 1993, pp. 609–619.
- [4] Saddington, A. J., Lawson, N. J., and Knowles, K., "Numerical Predictions and Experiments on Supersonic Jet Mixing from Castellated Nozzles," *23rd Congress of the International Council of the Aeronautical Sciences*, Toronto, Canada, 8–13 September 2002.
- [5] Saddington, A. J., Knowles, K., and Wong, R. Y. T., "Numerical Modelling of Mixing in Jets from Castellated Nozzles," *The Aeronautical Journal of the RAeS*, Vol. 106, No. 1066, December 2002, pp. 643–652.
- [6] Knowles, K. and Wong, R. Y. T., "Passive Control of Entrainment in Supersonic Jets," *RAeS Aerodynamics Research Conference*, London, 17–18 April 2000, pp. 9.1–9.14.
- [7] Saddington, A. J., Lawson, N. J., and Knowles, K., "Simulation and Experiments on Under-expanded Turbulent Jets," *CEAS Aerospace Aerodynamics Research Conference*, Cambridge, UK, 10–13 June 2002.
- [8] Wong, R. Y. T., *Enhancement of Supersonic Jet Mixing*, Ph.D. thesis, Department of Aerospace, Power and Sensors, Cranfield University, July 2000.
- [9] Rodi, W., *Turbulence Models and their Application in Hydraulics - A State of the Art Review*, International Association for Hydraulic Research, Rotterdamseweg 185 - P.O. Box 177, 2600 MH Delft, The Netherlands, 2nd ed., 1984.
- [10] Yakhot, A. and Orszag, S. A., "Renormalisation Group Analysis of Turbulence: I. Basic Theory," *Journal of Scientific Computing*, Vol. 1, No. 1, 1986, pp. 1–51.
- [11] Knowles, K. and Saddington, A. J., "Modelling and Experiments on Underexpanded Turbulent Jet Mixing," *5th International Symposium on Engineering Turbulence Modelling and Measurement*, Mallorca, Spain, 16–18 September 2002.
- [12] Ritchie, S. A., Lawson, N. J., and Knowles, K., "An Experimental and Numerical Investigation of an Open Transonic Cavity," *21st AIAA Applied Aerodynamics Conference*, Orlando, Florida, USA, 23–26 June 2003, Paper No. 2003-4221.
- [13] Hart, D. P., "PIV error correction," *Experiments in fluids*, Vol. 29, No. 1, 2000, pp. 13–22.
- [14] Meinhart, C., Wereley, S., and Santiago, J., "A PIV Algorithm for Estimating Time-Averaged Velocity Fields," *Journal of Fluids Engineering*, Vol. 122, No. 2, June 2000, pp. 285–289.
- [15] Lawson, N. J., Coupland, J. M., and Halliwell, N. A., "A Generalised Optimisation Method for Double Pulsed Particle Image Velocimetry," *Optics and Lasers in Engineering*, Vol. 27, No. 6, August 1997, pp. 637–656.
- [16] Hackett, J. E., Baker, J. B., Williams, J. E., and Wallis, S. B., "On the influence of ground movement and wheel rotation in tests on modern car shapes," Paper 870245, Society of Automotive Engineers, 1987.
- [17] Skea, A. F., Bullen, P. R., and Qiao, J., "The Use of CFD to Predict the Air Flow Around a Rotating Wheel," *2<sup>nd</sup> MIRA Int. Vehicle Aerodynamics Conf*, UK, 1998.
- [18] Basara, B., Beader, D., and Przulj, V. P., "Numerical Simulation of the Airflow around a Rotating Wheel," *3rd MIRA Int. Vehicle Aerodynamics Conf*, UK, 2000.
- [19] Axon, L., Garry, K., and Howell, J., "An Evaluation of CFD for Modelling the Flow Around Stationary and Rotating Isolated Wheels," Paper 980032, Society of Automotive Engineers, 1998.
- [20] Fackrell, J. E., *The Aerodynamic Characteristics of an Isolated Wheel Rotating in Contact with the Ground*, Ph.D. thesis, Imperial College of Science and Technology, London, 1972.
- [21] Fackrell, J. E. and Harvey, J. K., "The Flow Field and Pressure Distribution of an Isolated Road Wheel," *Advances in Road Vehicle Aerodynamics*, Paper 10, BHRA, London, 1973, pp. 155–165.
- [22] Knowles, R. D., Saddington, A. J., and Knowles, K., "Simulation and Experiments on an Isolated Road Wheel Rotating in Ground Contact," *4th MIRA International Vehicle Aerodynamics Conference*, Warwick, UK, 16–17 October 2002.
- [23] Makowski, F. T. and Kim, S.-E., "Advances in External-Aero Simulation of Ground Vehicles Using the Steady RANS Equations," *Vehicle Aerodynamics SP-1524*, Paper 2000-01-0484, Society of Automotive Engineers, 2000.
- [24] Hinson, M., *Measurement of the Lift Produced by an Isolated, Rotating Formula One Wheel Using a New Pressure Measurement System*, MSc thesis, Cranfield University, 1999.